Indian Journal of Engineering & Materials Sciences
Vol. 32, October 2025, pp. 655-662
DOI: 10.56042/ijems.v32i05.22480

*RAPID COMMUNICATION*

# Asymmetric Magnetoresistance and Topological Hall Effect in MnZnSb single crystal

Jai Dev[a,b], Navneet Kumar Karn[a,b], Surinder Pal Singh[a,b], Ajay Kumar Shukla[a,b] , & Pallavi Kushwaha[a,b*]

[a]CSIR-National Physical Laboratory, Dr. K.S. Krishnan Marg, New Delhi 110 012, India

[b]Academy of Scientific and Innovative Research (AcSIR), Ghaziabad 201 002, India

*Received: 01 May2025; accepted: 23 May2025*

The realization of advanced spintronic phenomena in bulk materials offers a robust alternative to complex thin-film heterostructures. This study investigates the low-temperature magnetic and magneto-transport properties of bulk single-crystal MnZnSb, a ferromagnet with a Curie temperature ($T_C$) of ~315 K. Comprehensive characterization reveals a complex magnetic ground state, defined by the coexistence of ferromagnetic (FM) clusters within an antiferromagnetic (AFM) or weak ferrimagnetic (WFRI) matrix. This state, stabilized by intrinsic features such as antisite disorder and kinetic arrest, creates a network of internal magnetic interfaces. Consequently, the material exhibits a pronounced spin-valve-like magnetoresistance (SVMR), an effect exceptionally rare in bulk systems, driven by spin-dependent scattering across these interfaces. Concurrently, we uncover a significant topological Hall effect (THE), with a topological Hall resistivity ($\rho_{XY}^{T}$) of ~440 nΩ-cm at 5 K, contradicting earlier reports of its absence. The SVMR and THE are presented as complementary transport signatures of the non-trivial spin textures arising from the material's intrinsic magnetic inhomogeneities. These findings demonstrate that complex, heterostructure-like spintronic functionalities can emerge from phase competition in a single bulk material, opening new avenues for device design.

**Keywords**: Asymmetric magnetoresistance, Interface magnetism, Kinectic Arrest, Topological Hall Effect

## 1 Introduction

The pursuit of multifunctional materials capable of hosting diverse and advanced physical phenomena is a central theme in condensed matter physics, with profound implications for next-generation spintronics. Properties such as room-temperature ferromagnetism[1], giant magneto resistance (GMR)[2], and the emergence of topological states like skyrmion lattices[3-6] are critical for technological innovation[7]. While significant progress has been achieved in thin-film heterostructures, where phenomena like tunnelling magneto resistance (TMR) are engineered through precise layer-by-layer growth, the exploration of analogous effects in bulk materials remains a formidable challenge[8-9].

One such phenomenon, the spin-valve-like magneto resistance (SVMR), which manifests as a change in electrical resistance due to the relative alignment of magnetic regions, was first discovered in multilayer systems[10-11]. Its observation in bulk materials[12-16] is exceptionally rare, hindered by crystallographic defects, uncontrolled domain structures, and the difficulty in engineering the sharp magnetic interfaces and the inherent protection of topological states[15]. A promising pathway to overcome this limitation is to exploit intrinsic magnetic phase coexistence, where competing magnetic orders at the microscopic scale can naturally form the necessary interfaces within a single-phase bulk crystal.

Earlier studies show that the phase boundary plays a crucial role in the appearance of SVMR in the case of heterostructures[14]. In analogy to thin film, a phase boundary could exist in bulk via magnetic phase coexistence at a microscopic length scale[17]. To explore the existence of SVMR in bulk material, Mn-based compounds, especially $Mn_2Sb$ family compounds could be suitable due to the availability of multiple oxidation states and the high magnetic moment[18-19] which creates intriguing properties like anomalous Hall effects (AHE), topological Hall effects (THE), skyrmion formation, magnetocaloric effects (MCE), 2D magnetism etc.[20-22]. Two different crystallographic positions of Mn atoms (Mn(I) and Mn(II)) form a triple-layer arrangement in such a manner that one triple layer aligns parallel to each other, resulting in ferrimagnetic (FRI) ordering below

*Corresponding author (Email: pallavik.nplindia@csir.res.in)

550 K, followed by a spin reorientation transition near 240 K[23]. Mn as well as Sb site substituted by transition elements, i.e, $Mn_{2-x}Sb_yT_{x/y}$ (T=Cr, Co, Zn, V, Fe, Ge, Bi, Sn, etc.), modifies structural parameters resulting in different magnetic phases due to coupled electrical, magnetic, and lattice degrees of freedom[22,24-30]. Among the transition metal substitutions, Zn doping in $Mn_{2-x}Zn_xSb$ introduces unique opportunities to control magnetic phases by carefully tuning the Zn concentration in the crystal lattice[24,31]. Specifically, the complete replacement of the Mn(II) atom by Zn in $Mn_2Sb$, i.e, MnZnSb, forces the system into a FM state, which results in many noticeable observations[32]. A detailed study has been performed by controlling Zn content in $Mn_{2-x}Zn_xSb$, which reveals the appearance of skyrmions in a narrow doping range only[21]. Careful observation reveals the presence of a broad hump-like structure below 150K in temperature-dependent magnetization behaviour, which could be a signature of a distinct magnetic state, possibly linked to phase coexistence or glass-like magnetic behaviour,which may result in the interesting transport properties in bulk material. However, the precise nature of these low-temperature magnetic states and their influence on magneto transport remains to be elucidated.

In this work, we present a comprehensive investigation into single-crystal MnZnSb, revealing how slight intrinsic inhomogeneities, such as antisite disorder, give rise to a complex low-temperature magnetic state characterized by kinetic arrest and phase coexistence. We demonstrate that this intrinsic magnetic landscape generates two remarkable and correlated magneto transport phenomena: an asymmetric, spin-valve-like magnetoresistance and a substantial THE. Our findings establish a critical link between microscopic magnetic disorder, emergent topological spin textures, and macroscopic transport properties, showcasing a viable route to achieving advanced spintronic functionalities in bulk crystalline materials.

## 2 Materials and Methods

### 2.1 Materials Synthesis

The synthesis of single-crystalline $Mn_2Sb$-based compounds is notably challenging due to the high vapour pressures of Mn and Sb. According to the binary phase diagram of the Mn-Sb system, the $Mn_2Sb$ phase forms through congruent melting at 948°C[33]. Even minor variations in composition can result in the formation of other phases, such as the more stable MnSb. To overcome these challenges, we employed a modified Bridgman method for the growth of single-crystalline MnZnSb compound. For the synthesis, high-purity elemental Mn (99.95%), Sb (99.999%), and Zn (99.99%) were weighed and combined in a stoichiometric ratio. These elements were placed in a pointed-bottom, cylindrical $Al_2O_3$ crucible, which was subsequently sealed within a quartz ampoule under a vacuum pressure of $10^{-5}$ mbar. The sealed quartz ampoule was subjected to heat treatment in a muffle furnace. To minimize the evaporation rate of the elements and achieve uniform homogeneity, the heat treatment process was divided into several stages. First, the sample was heated to 900°C in 72 hours, followed by a 24-hour hold. Then, it was heated to 960°C in 6 hours, with another 6-hour hold. The sample was then cooled to 850°C in 110 hours, and finally cooled to room temperature over 10 hours. This meticulous control of the temperature profile is essential for successfully synthesising single crystals of MnZnSb. A picture of the obtained crystal has been shown as the top left image in Fig. 1.

### 2.2. Experimental Methods

Powder X-ray diffraction (XRD) measurements were performed using a Rigaku diffractometer (Ultima-IV) equipped with Cu-Kα radiation (λ = 1.54 Å) at room temperature after grinding flakes of the single-crystalline sample. The same instrument was used for analyzing the cleaved bulk sample surface. Observed XRD patterns were analysed using the FULLPROF refinement program to determine the structural parameters. To study the crystallographic orientation, synthesised crystals are oriented using the

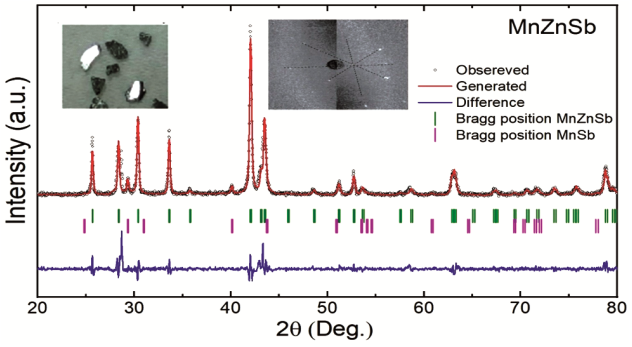


Fig. 1 — Images of bulk single crystals (top left image) grown with the modified Bridgeman technique. Laue diffraction pattern (top right image) taken on the shiny crystalline surface of the cleaved sample. Reitveld refinement of X-ray diffraction data collected on powder XRD at room temperature.

Laue diffraction technique using a tungsten target with x-ray wavelength from 0.5 Å to 4.2 Å. The diffraction patterns are collected on a photographic film in back reflection geometry. The stoichiometric ratio and homogeneous distribution of constituent elements on a cleaved surface of the synthesized single crystal were examined using Scanning Electron Microscopy (Tescan Magna GMH) and Energy Dispersive Analysis of X-ray (EDAX-Octane Elect Super). Magnetization as a function of temperature, magnetic field, and time was measured using a 7-Tesla Magnetic Property Measurement System (MPMS-XL, Quantum Design, USA) in both parallel and perpendicular directions to the applied magnetic field. The magneto-transport properties have been measured using the resistivity option in the 14-Tesla Physical Property Measurement System (PPMS, Quantum Design, USA). All electrical and magnetic measurements were performed on a bulk cleaved single-crystalline sample.

## 3 Result and Discussion

### 3.1 Structural analysis

Room temperature powder XRD analysis, shown in Fig. 1, confirms that the synthesized MnZnSb crystallizes in the anti-PbFCl type tetragonal structure with space group P4/nmm, consistent with JCPDS data (152-7599). Rietveld refinement of the observed powder XRD pattern was performed using the anti-PbFCl type crystal structure, space group of P4/nmm, and atomic positions for Mn (1/4,1/4,z); Sb (1/4,1/4, z') and Zn (3/4,1/4,0) with z/z' value of 0.273/0.72 respectively[34-35]. Refinement results show the lattice parameters a = 4.1605 Å and c = 6.2915 Å are in good agreement with the existing literature[32]. A minor secondary phase of magnetic MnSb (~3%) was also detected, which is a crucial detail given its potential contribution to magnetic in homogeneity. The Laue diffraction pattern taken on the flat surface of the crystal, shown as the top right image in Fig. 1, displays bright spots with four-fold symmetry, indicating the ab-plane of the tetragonal structure.

### 3.2 Microstructural and chemical analysis

To determine the chemical composition of the synthesized samples, EDAX measurements performed at multiple locations on the cleaved crystal surface determined an average atomic ratio of $Mn_{1.03}Zn_{0.99}Sb_{0.99}$, as shown in Fig. 2. This slight off-stoichiometry, particularly the Mn excess, suggests the presence of antisite disorder (e.g., Mn atoms occupying Zn sites), which is a known source of competing magnetic interactions in such intermetallic systems. Large area elemental mapping confirmed a macroscopically uniform distribution of all constituent elements, indicating that these compositional variations occur at the local or microscopic level.

### 3.3 Magnetic and Magneto-transport properties characterisation

To probe the magnetic ground state, temperature-dependent magnetization (M-T) was measured in the presence of the magnetic field. For the zero-field-cooled warming (ZFCW) measurement, the sample was initially cooled from room temperature down to 2 K in the absence of any externally applied magnetic field. Once the sample reached 2 K, a magnetic field of 100 Oe was applied isothermally, and data were recorded during the subsequent warming cycle up to 325 K. Following the ZFCW process, successive field-cooled cooling (FCC) and field-cooled warming cycles (FCW) were conducted in the presence of a labeled constant magnetic field. The magnetization as a function of temperature (M-T) was measured while applying a magnetic field parallel to c-axis and ab-plane as shown in Fig. 3 (a & b), respectively.

Figure 3(a) and (b) illustrate the isofield magnetization measurements conducted in two orientations: with the external magnetic field aligned parallel (H || c) and perpendicular (H || ab) to the crystallographic c-axis. A clear bifurcation between the zero-field-cooled (ZFC) and field-cooled (FC) curves is observed in both orientations, which is a classic signature of magnetic frustration, disorder, or glassy behaviour. For the H || c orientation, a sharp decrease in magnetisation is observed near 315 K, which corresponds to the Curie temperature ($T_c$). This transition marks the onset of a second-order magnetic phase (SOMP) transition from the FM state to the paramagnetic (PM) state as the temperature increases. In contrast, the H || ab orientation does not exhibit a complete magnetic transition within the given temperature range, suggesting significant magnetic anisotropy in the synthesised sample.

This anisotropy is further confirmed through isothermal magnetisation measurements performed at 250 K and 5K as shown in Fig. 3 (c). In case of H || c configuration, the magnetisation saturates at relatively low magnetic fields, indicating that the c-axis serves as the easy axis of magnetisation.

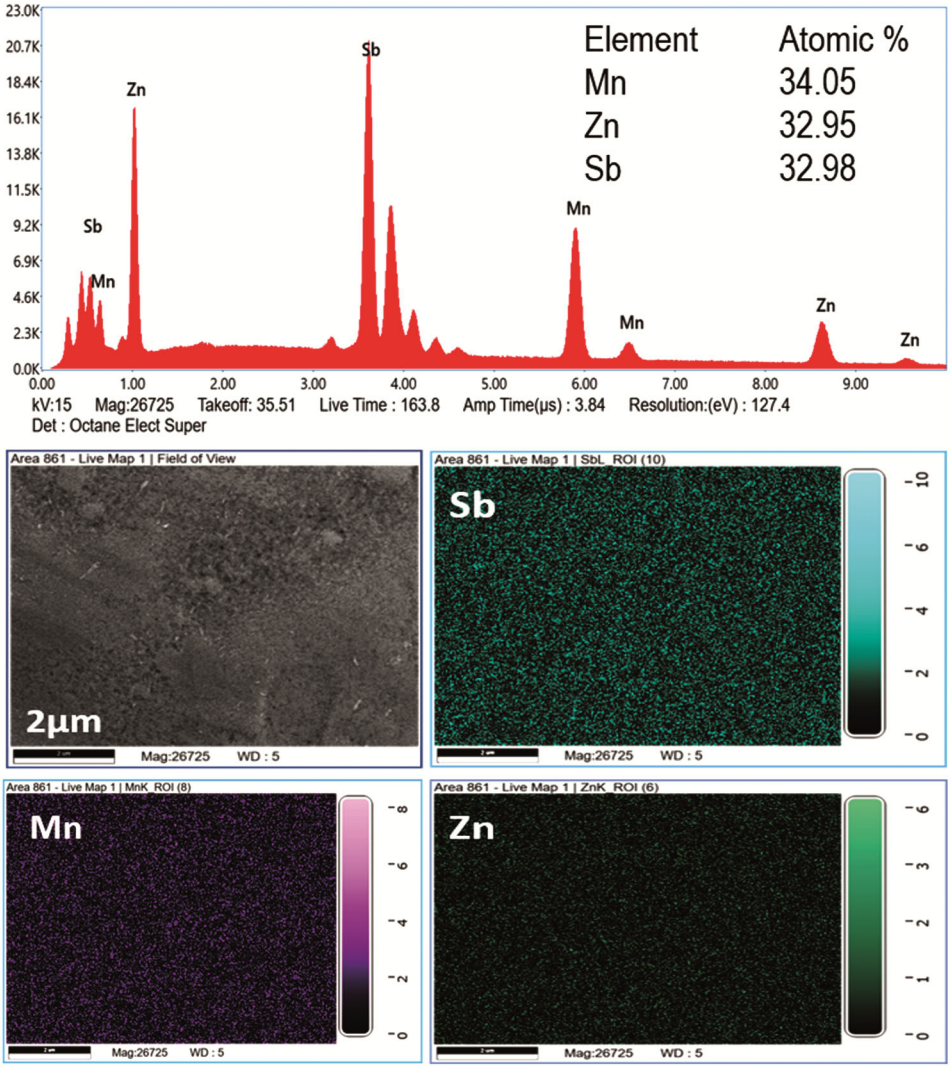


Fig. 2 — (Top) EDAX spectra and (bottom clockwise) SEM images along with corresponding elemental mapping of Sb, Zn, and Mn elements present in the prepared single crystalline MnZnSb.

An enlarged low-temperature magnetisation data (inset of Fig. 3 (a)) shows the presence of thermal hysteresis in FCC and FCW above 50 K with crossover behaviour. A small hysteresis between the FCC and FCW curve suggests a first-order-like magnetic transition (FOMP) into a distinct low-temperature state, such as a weak ferrimagnetic (WFRI) or antiferromagnetic (AFM) phase.

In the current study, the calculated magnetic moment is 1.1 $\mu_B$/Mn, which is close to the reported range of 1.5-1.2 $\mu_B$/Mn[32,35-36]. This variation in magnetic moment could be attributed to chemical in homogeneity or site disorder at the local level, specifically due to the possibility that the Mn(II):Zn ratio might not always maintain the ideal 1:1 stoichiometry. The asymmetric distribution of Zn over Mn(II) within the crystal lattice could introduce different magnetic interactions at the local level, giving rise to multiple magnetic states with varying temperatures[20-21]. The existence of such multiple intermediate magnetic states has been well established in Cr and Co-doped $Mn_2Sb$ in the dilute limit[37-38]. The presence of intermediate magnetic state (WFRI/AFM) in the present study could be expected due to very little change in magnetisation, along with the existence of bifurcation.

Such compositional studies conducted on present material further support the hypothesis, as they clearly indicate the emergence of a WFRI/AFM state. Keeping in view the anisotropic nature of the material, further magnetic measurements in this study were conducted with the magnetic field aligned parallel to the c-axis, i.e, easy axis. This alignment

emphasizes the dominant magnetic interactions along this axis and provides deeper insights into the material's anisotropic magnetic properties.

The electrical resistivity, shown in Fig. 3(d), confirms the strong coupling between magnetic and electronic degrees of freedom, exhibiting a clear anomaly at $T_c$. Below the transition, the material displays metallic behaviour. The application of a 7T magnetic field suppresses the magnetic ordering, leading to a negative magnetoresistance, which is characteristic of the suppression of spin-disorder scattering in ferromagnetic metals.

The complex nature of this low-temperature state is further elucidated by time-dependent magnetisation

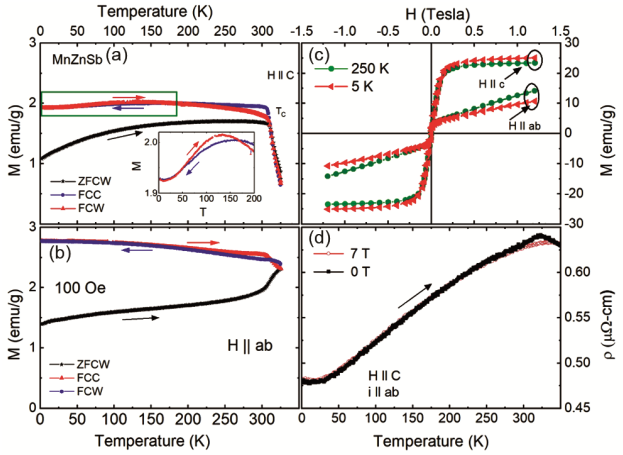


Fig. 3 — Magnetization as a function of temperature in different crystallographic directions (a) H || c, and (b) H||ab . The inset in (a) shows the magnified view of the boxed M-T region. (c) isothermal magnetization at 5K and 250 K, and (d) resistivity in the presence of a labelled external magnetic field.

relaxation measurements, as shown in Fig. 4. All measurements shown in Fig. 4 have been collected after cooling the sample from 325 K in the presence of a 2T magnetic field. The field was then set to zero isothermally in oscillation mode, and relaxation was recorded over 20000 seconds. The same protocol was used for data collection at each labelled temperature. The cooling field of 2T has been decided after performing isothermal magnetisation at different temperatures (Fig. 3(c)), which shows the magnetic moment saturates above 1.5T.

The relaxation data shown in Fig. 4 were fitted with a combination of power law and stretched exponential equations $M_t/M_0 = A(T)\,(-1 + 2t^{\gamma}) + B(T)\,(\exp(-(t/\tau)^{\beta}))$, which is typically used to describe glassy systems with coexisting magnetic clusters (where A and B: temperature dependent weight factors, and $\gamma$, $\tau$ and $\beta$ are the extent of relaxation, characteristic relaxation time and a shape parameter respectively). This kinetic arrest prevents the system from reaching its true thermodynamic ground state (likely AFM/WFRI) on experimental time scales, resulting in a metastable phase where FM clusters are frozen within a majority AFM/WFRI matrix. The most significant drop in normalised magnetisation occurs around 80 K (Fig. 4(b)), marking the onset of this super cooled, phase-separated state. The fitted parameters are within the limits required for phase coexistence ($\gamma$=-ve, $\beta$=0.6- 0.9)[39-41]. These findings are in good agreement with existing literature in the field[39-41]. Here, observation of a kinetically arrested state with coexisting FM and AFM/WFRI clusters

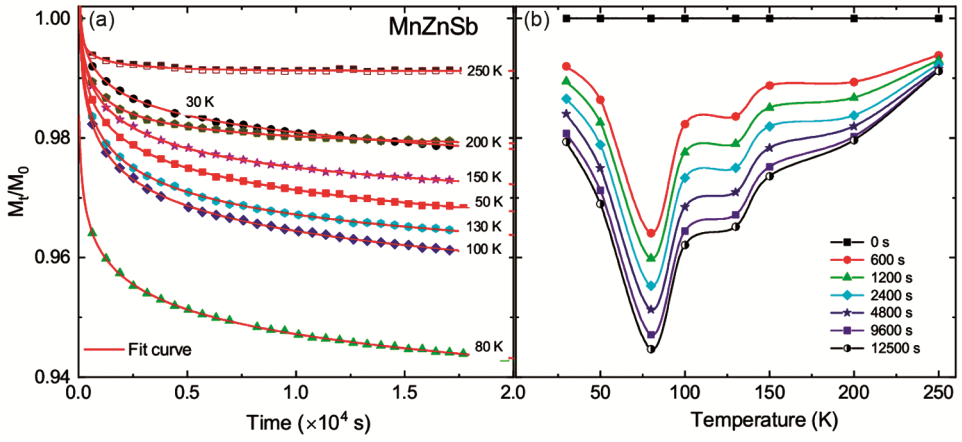


Fig. 4 — (a) Normalized magnetization ($M_t/M_0$) as a function of time at labelled temperature measured in the absence of magnetic field after following FCC protocol at 2T. Symbols are the observed data, and the solid line is the fitting data using the power law and the stretched exponential equation, and (b) For easy visualization, normalised magnetization was also plotted as a function of temperature at different times of relaxation.

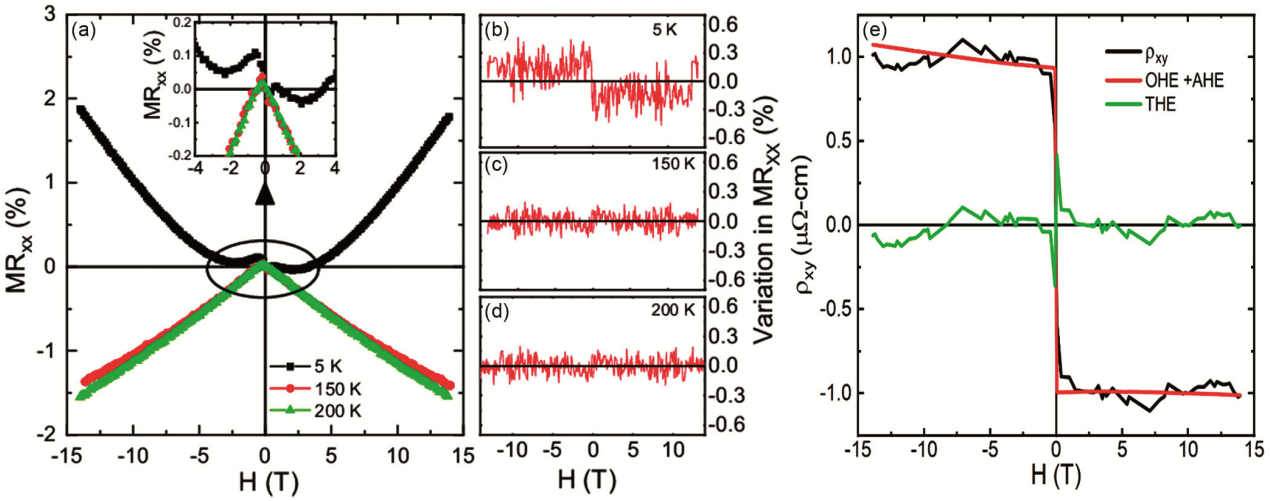


Fig. 5 — (a) Magnetic field dependence of the $MR_{XX}$ at different temperatures, (b-d) Asymmetric component of $MR_{XX}$ at 5K, 150K, and 200K. The inset in (a) demonstrates the magnified view of the encircled region, and (e) The obtained ordinary, anomalous, and the topological Hall resistivity at T = 5 K.

provides the necessary ingredients (interfaces and switchable magnetic entities) to look at the electrical magneto transport characteristics of the material.

The complex, phase-separated magnetic ground state gives rise to remarkable magnetotransport phenomena that are highly unusual for a bulk material. Isothermal longitudinal magnetoresistance ($MR_{xx}$) measurements were performed at different temperatures, as shown in Fig. 5(a).

At 300 K, $MR_{XX}$ exhibits a negative trend, confirming the FM state. With decreasing temperature, the magnitude of MR diminishes, accompanied by an anomalous asymmetric variation as a function of the polarity of the applied magnetic field. Notably, the degree of asymmetry increases as the temperature decreases, as illustrated in Fig. 5(a). This behaviour, known as SVMR, is exceptionally rare in bulk materials and is typically associated with spin-dependent transport across interfaces in multilayered thin films[11]. In addition, bulk materials such as $Mn_2NiGa$ and $Mn_2PdSn$ also show such behaviour, where two distinct resistance states can be switched by reversing the direction of the magnetic field. By decomposing the MR into symmetric and asymmetric components using [MR(H)-MR(-H)]/2 and [MR(H)+MR(-H)]/2, respectively[15], we quantify the SVMR effect, which reaches a maximum of ~0.2% at 5 K as shown in Fig. 5 (b-d) and vanishes at higher temperatures where the phase coexistence melts away. This observation provides compelling evidence that the intrinsic magnetic interfaces formed between the FM clusters and the AFM/WFRI matrix effectively simulatea spin-valve system.

To further probe the nature of the spin texture, Hall resistivity ($\rho_{XY}$) was measured as shown in Fig. 5 (e). The total Hall resistivity can be expressed as the sum of three contributions: the Ordinary Hall effect (OHE), the Anomalous Hall effect (AHE), and the Topological Hall effect (THE)

$$\rho_{XY} = R_{\circ} H + S_H \rho_{XX}^2 M_{sat} + \rho_{XY}^T$$

where $R_{\circ}$, and $S_H$ are the coefficients, $M_{sat}$, and $\frac{\rho_{XX}}{\rho_{XY}}$ are the saturation magnetisation and longitudinal /transverse resistivity, respectively. The first term denotes the ordinary hall resistivity ($\rho^{\circ}_{XY} = R_{\circ} H$), the second termis anomalous hall resistivity ($\rho_{XY}^A = S_H \rho_{XX}^2 M_{sat}$) typically arising from spin-orbit coupling, and the last is the topological Hall resistivity ($\rho_{XY}^T$). The coefficients were calculated by the linear fitting of $\frac{\rho_{XY}}{H}$ with $\frac{\rho_{XX}^2 M}{H}$, the intercepts give the value of $R_{O,}$ and the slope gives the value of $S_H$. With these values, we can have the $\rho^{\circ}_{XY}$ and $\rho_{XY}^A$ also, by subtracting the $\rho^{\circ}_{XY}$ and $\rho_{XY}^A$ from the $\rho_{XY}$. We can extract the topological contribution to the Hall resistivity.

In contrast to previous studies that reported negligible THE in MnZnSb, our analysis reveals a clear topological signature, with a substantial $\rho_{XY}^T \approx$ 440 nΩ-cm at 5 K. This discrepancy may be attributed to intrinsic in homogeneities, such as antisite disorder and the presence of a secondary magnetic phase, both of which were confirmed through structural and magnetic characterizations. These magnetic inhomogeneities can replicate the THE-like signal,

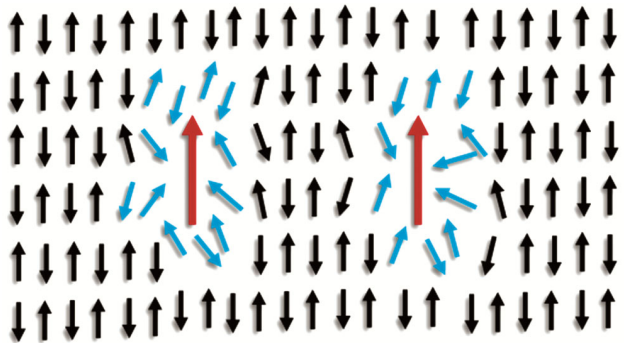

Fig. 6 — Schematic diagram of MnZnSb showing the localized magnetic spins arrangements. The red arrows demonstrate the FM clusters in the AFM (black arrows) matrix below the transition temperature. Blue arrows are the magnetic spins at the interface of the FM and AFM matrix.

often referred to as "artificial THE"[42-43], arising from phase-separated regions with non-collinear spin structures. These findings not only expand the understanding of topological effects in Mn-based compounds but also highlight the role of disorder and phase coexistence in stabilizing unconventional transport phenomena.

Our comprehensive experimental results converge to a unified physical picture, schematically illustrated in Fig. 6. The intrinsic chemical disorder (Mn/Zn antisites) in the MnZnSb crystal lattice induces competing magnetic interactions. At low temperatures, this leads to a kinetically arrested state characterised by the coexistence of nanoscale FM clusters embedded within a larger AFM/WFRI matrix.

This heterogeneous magnetic landscape provides the necessary ingredients for the observed emergent transport phenomena. The SVMR arises from spin-dependent scattering of conduction electrons at the numerous interfaces between the FM clusters and the surrounding matrix. When an external magnetic field is applied, the magnetisation of the FM clusters can be reoriented more readily than the rigid AFM/WFRI background. This change in the relative alignment of magnetization across the interfaces modulates the scattering rate, leading to a change in resistance. The asymmetry of this effect with respect to field polarity is a direct consequence of the hysteretic and asymmetric switching of these FM clusters.

Simultaneously, the disordered and canted spins at these same interfaces create a non-coplanar spin texture. This texture generates a non-zero real-space Berry curvature, which acts as an emergent magnetic field on the conduction electrons, giving rise to the observed THE. Therefore, the SVMR and THE are not independent phenomena but are rather two distinct and complementary electronic signatures of the same underlying complex, phase-separated magnetic state.

## 4 Conclusion

The present study establishes a compelling correlation between AMR, SVMR, and THE in bulk single-crystalline MnZnSb. Below 150 K, magnetic and transport measurements reveal the coexistence of FM clusters within a weakly WFRI/AFM matrix, a configuration likely induced by antisite disorder and kinetic arrest. This magnetic phase separation creates internal interfaces across where spin-dependent scattering governs transport, giving rise to pronounced SVMR behaviour, reaching up to 0.2% at 5 K. Concurrently, the detection of a non-negligible $\rho_{XY}^{T} \approx 440$ nΩ-cm confirms the presence of non-trivial spin textures—likely rooted in local spin canting or topological configurations there by establishing a critical link between real-space spin topology and magneto-transport. The observation of SVMR, reaching up to 0.2% at 5 K, while modest in its current manifestation, represents a significant scientific proof-of-concept, particularly given the rarity of such effects in bulk material systems. The path forward necessitates a concerted effort involving advanced microstructural and element-specific magnetic characterization to solidify the proposed mechanism, coupled with sophisticated theoretical modelling incorporating local disorder and spin-orbit coupling. Simultaneously, systematic materials engineering through controlled stoichiometry, doping, and strainis imperative to enhance the SVMR magnitude and elevate the operating temperature, thereby assessing its practical viability for future spintronic devices such as novel magnetic sensors or memory elements.

## Acknowledgement

Jai Dev, expresses deep gratitude for the financial support provided by the Council of Scientific and Industrial Research (CSIR), India, through the CSIR-SRF program (Budget Head-P-81101). The authors thank the Director NPL, New Delhi, for internal funding (OLP230532 and INF202508). Dr. Jai Tawale is acknowledged for performing the EDAX/SEM measurements.

## References

1 Singh S, Kumar V, Tyagi S, Saxena N, Khan Z H & Kumar P, Opt Quant Electron, 55 (2023) 123.
2 Zabel H, Superlattice Microst, 46 (2009) 541-553.

3 Saerbeck T, Venta J D L, Wang S, Ramírez J G, Erekhinsky M, Valmianski I & Schuller I K, J Mater Res, 29 (2014) 2353-2365.
4 Meseguer-Sánchez J, Popescu C, García-Muñoz J L, Luetkens H, Taniashvili G, Navarro-Moratalla E, Guguchia Z & Santos E J G, Nat Commun, 12 (2021) 6265.
5 Fert A, Reyren N & Cros V, Nat Rev Mater, 2 (2017) 17031.
6 Vidal R C, Zeugner A, Facio J I, Ray R, Haghighi M H, Wolter A U B, Corredor Bohorquez L T, Caglieris F, Moser S, Figgemeier T, Peixoto T R F, Vasili H B, Valvidares M, Jung S, Cacho C, Alfonsov A, Mehlawat K, Kataev V, Hess C, Richter M, Büchner B, Brink J V D, Ruck M, Reinert F, Bentmann H & Isaeva A, Phys Rev X, 9 (2019) 041065.
7 Smejkal L, Mokrousov Y, Yan B & MacDonald A H, Nat Phys, 14 (2018) 242-251.
8 Ishikawa T, Marukame T, Kijima H, Matsuda K I, Uemura T, Arita M & Yamamoto M, Appl Phys Lett, 89 (2006) 192505.
9 Falicov L M, Pierce D T, Bader S D, Gronsky R, Hathaway K B, Hopster H J, Lambeth D N, Parkin S S P, Prinz G, Salamon M, Schuller I K & Victora R H, J Mater Res, 5 (1990) 1299-1340.
10 Baibich M N, Broto J M, Fert A, Dau F N V & Petroff F, Phys Rev Lett, 61 (1988) 21.
11 Dieny B, Sperious V S, Parkin S S P, Gurney B A, Wilhoit D R & Mauri D, Phys Rev B, 43 (1991) 1297.
12 Cao G, Durairaj V, Chikara S, DeLong L E, Schlottmann P, Phys Rev Lett, 100 (2008) 016604.
13 Singh S, Rawat R, Muthu S E, D'Souza S W, Suard E, Senyshyn A, Banik S, Rajput P, Bhardwaj S, Awasthi A M, Ranjan R, Arumugam S, Schlagel D L, Lograsso T A, Chakrabarti A & Barman S R, Phys Rev Lett, 109 (2012) 246601.
14 Samanta T, Saleheen A U, Lepkowski D L, Shankar A, Dubenko I, Quetz A, Khan M, Ali N & Stadler S, Phys Rev B, 90 (2014) 064412.
15 Bhattacharya A, Habib M R, Ahmed A, Satpati B, DuttaGupta S, Dasgupta I, Das I, Phys Rev B, 110 (2024) 014417.
16 Bae H, Gajek M, Bibes M, Barthelemy A, J Phys Condens Matter, 20 (2008) 434221.
17 Dieny B, J MagnMagn Mater, 136 (1994) 335-359.
18 Patel K, Zhang J, Ren S, Nanoscale, 10 (2018) 11701-11718.
19 Brück E, Tegus O, Thanh D T C, Trung N T, Buschow K H J, Int J Refrig, 31 (2008) 763–770.
20 Nabi M R U, Basnet R, Pandey K, Chhetri S K, Upreti D, Acharya G, Wang F, Fereidouni A, Churchill H O H, Guan Y, Mao Z, Hu J, Acta Mater, 259 (2023) 119251.
21 Nabi M R U, Wegner A, Wang F, Zhu Y, Guan Y, Fereidouni A, Pandey K, Basnet R, Acharya G, Churchill H O H, Mao Z, Hu J, Phys Rev B, 104 (2021) 174419.
22 Dinkar D K, Palit M, Gopalan R, Das B, J Magn Magn Mater, 489 (2019) 165437.
23 Wilkinson M K, Gingrich N S, Shull C G, J Phys Chem Solids, 2 (1957) 289-300.
24 Val'kov V I, Golovchan A V, Bribanov I F, Kamenev V I, Iesenchuk O O, Sivachenko A P, Kabdin N N, Low Temp Phys, 33 (2007) 70-78.
25 Harada T, Hasebe Y, Mori S, Nishimura K, Kanomata T, Kaneko T, Int J Mod Phys B, 7 (1993) 879-882.
26 Wijngaard J H, Haas C, de Groot R A, Phys Rev B, 45 (1992) 5395.
27 Kushwaha P, Rawat R, Chaddah P, J Phys Condens Matter, 20 (2008) 022204.
28 Cui W, Ren W, Zhang Z D, Zhou X, Zhong H, Wang Q, Scripta Mater, 143 (2018) 59-62.
29 Matsumoto Y, Matsubayashi K, Uwatoko Y, Hiroi M, Mitsui Y, Koyama K, AIP Conf Proc, 1763 (2016) 020005.
30 Blaauw C, MacKay G R, Leiper W, J MagnMagn Mater, 8 (1978) 240-248.
31 Ryzhkovskii V M, Mitsiuk V I, Inorg Mater, 46 (2010) 581-586.
32 Pankratov N Y, Mitsiuk V I, Ryzhkovskii V M, Nikitin S A, J Magn Magn Mater, 470 (2019) 46–49.
33 Kainzbauer P, Richter K W, Ipser H, J Phase Equilib Diffus, 37 (2016) 4.
34 Rietveld H, J Appl Cryst, 2 (1969) 65.
35 Johnson V, Jeitschko W, J Solid State Chem, 22 (1977) 71-75.
36 Murgatroyd P A E, Routledge K, Durdy S, Gaultois M W, Surta T W, Dyer M S, Claridge J B, Savvin S N, Pelloquin D, Hébert S, Alaria J, Adv Funct Mater, 31 (2021) 2100108.
37 Darnell F J, Cloud W H, Jarrett H S, Phys Rev, 130 (1963) 647.
38 Wilden J S, Hoser A, Chikovani M, Perßon J, Voigt J, Friese K, Grzechnik A, Inorganics, 6 (2018) 113.
39 Chattopadhyay M K, Roy S B, Chadhah P, Phys Rev B, 18 (2007) 180401.
40 Brawer S A, J Chem Phys, 81 (1984) 1026-1036.
41 Chen J, Gao Y, Wu L, Ma J, Nan C, Mater Res Lett, 5 (2016) 329-334.
42 He Y, Kroder J, Gayles J, Fu C, Pan Y, Schnelle W, Felser C, Fecher G H, Appl Phys Lett, 117 (2020) 052409.
43 Fu T, Li S, Feng X, Cui Y, Yao J, Wang B, Cao J, Shi Z, Xue D, Fan X, Phys Rev B, 103 (2021) 064432.